The varying densification strain in a multi-layer aluminum corrugate structure: Direct impact testing and layer-wise numerical modelling

CrossMark

İsmet Kutlay Odacı, Mustafa Güden*, Cenk Kılıçaslan, Alper Taşdemirci

Dynamic Testing and Modeling Laboratory and Department of Mechanical Engineering, Izmir Institute of Technology, Gülbahçe Köyü, Urla, Izmir, Turkey

A B S T R A C T

An aluminum (1050 H14) multi-layer corrugated structure composed of brazed 16 trapezoidal zig-zig fin layers was direct impact tested above the critical velocities for shock formation using a modified Split Hopkinson Pressure Bar. The experimentally measured stress-time histories of the cylindrical test samples in the direct impact tests were verified with the simulations implemented in the explicit finite element code of LS–DYNA. The quasi-static experimental and simulation deformation of the corrugated samples proceeded with the discrete, non-contiguous bands of crushed fin layers, while the dynamic crushing started from the proximal impact end and proceeded with a sequential and in-planar manner, showing shock type deformation characteristic. The experimental and numerical crushing stresses and the numerically determined densification strains of the fin layers increased with increasing impact velocity above the critical velocities. When the numerically determined densification strain at a specific velocity above the critical velocities was incorporated, the rigid-perfectly-plastic-locking idealized model resulted in peak stresses similar to the experimental and simulation mean crushing stresses. However, the model underestimated the experimental and simulation peak stresses below 200 m s^{-1}. It was proposed, while the micro inertial effects were responsible for the increase of the crushing stresses at and below subcritical velocities, the shock deformation became dominant above the critical velocities.

© 2016 Elsevier Ltd. All rights reserved.

1. Introduction

The direct impacting of cellular materials and structures to the rigid walls/targets, for example wood [1,2], urethane foam [3], aluminum foam [4] and aluminum honeycomb [5], results in the development of shock stress at the proximal end when the velocity is over a critical value [6]. The shock stress wave propagation from the proximal end transforms the low velocity crushing mode of discrete and non-contiguous bands into sequential and planar bands [5,7]. The stress developed during the impact is also much higher than that of the quasi-static and increases with increasing impact velocity. One of the earliest analytical approach to the shock development in cellular materials/structures is the rigid perfectly plastic locking (r-p-p-l) idealization model developed by Reid and Peng in 1997 [1]. In this model, the cellular structure with an infinite elastic modulus is assumed to exhibit a constant plateau/crushing stress and a densification strain. The r-p-p-l idealized model was successfully applied to wood (e.g. [2]), aluminum foam (e.g. [4,7]) and aluminum honeycomb (e.g. [5,8]). The model details can be found in Refs. [1,4]. Later, elastic-perfectly-plastic-rigid [9], elastic and rigid softening hardening [2], strain hardening [10] and rigid power law hardening [11] material models have

been implemented in order to elaborate further the shock wave propagation in cellular materials and structures. The recent studies have also indicated an impact velocity dependent densification strain as the crushing stress in cellular structures [5,12–13].

The dispersion in the strength of aluminum closed-cell foams widely used in shock wave propagation studies [4,9,14–16] was reported in the order of 20% [14]. The dispersion may cover the increase in strength at increasing strain rates/velocities. The reported opposing strain rate sensitivities of aluminum closed-cell foams in the literature were partly attributed to the dispersion in the strength values [17]. The multi-layer corrugated structures in trapezoidal and triangular forms, on the other side, are homogenous in structure and were previously reported to show repeatable responses to the quasi-static and dynamical mechanical loads [18–21]. These structures allow the accurate determination of strain rate effect on mechanical properties. It is also possible to construct 3D full models with these structures in order to monitor velocity and strain variations in each layer. In this study a 1050 H14 Al multi-layer corrugated structure of 16 brazed trapezoidal zig-zig fin layers was direct impact tested in a modified Split Hopkinson Pressure Bar (SHPB) above the critical velocities (>100 m s^{-1}) in order to determine numerically the change of densification strain with impact velocity. The stress-time histories of the direct impact tests above the critical velocities (105, 140 and 200 m s^{-1}) were verified with the
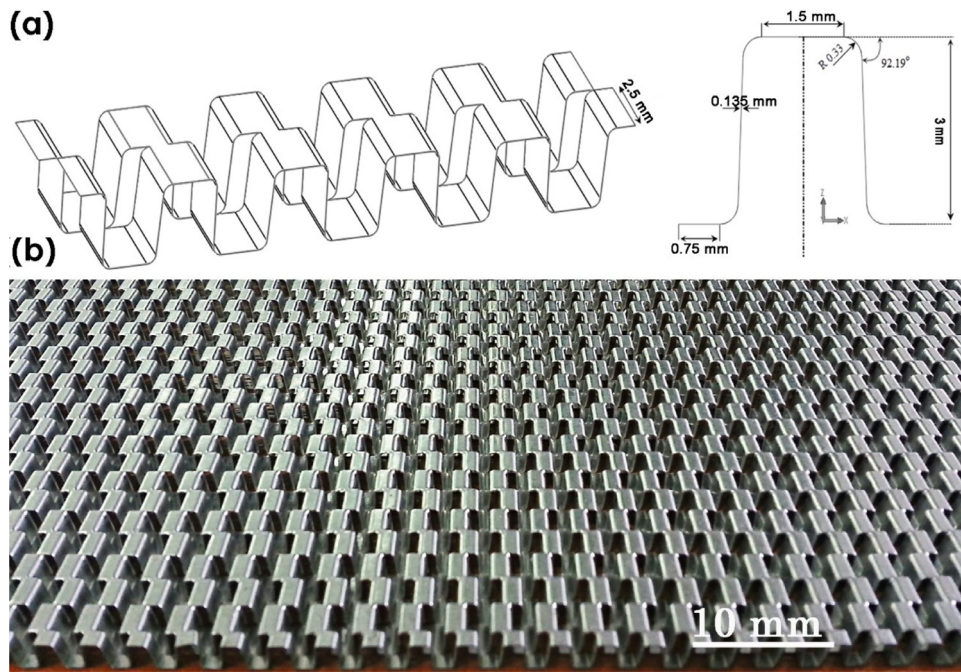
Fig. 1. (a) The geometry of the fins and (b) the isometric picture of a corrugated fin layer.

simulations in the explicit finite element code of LS-DYNA. Once the tests were verified, the direct impact test simulations at lower and higher impact velocities were implemented. The simulation results showed that the densification strain was velocity dependent and increased with the increasing impact velocity above the critical velocities. The r-p-p-l model stresses of the corrugated sample were calculated using both the numerically determined velocity-dependent densification strains and quasi-static densification strain. Results showed that the r-p-p-l model peak stresses calculated using the numerically determined densification strains were well correlated with the experimental and simulation mean stresses, while the r-p-p-l model peak stresses calculated using the quasi-static densification strain well predicted the peak stresses at and above 200 m s^{-1}.

2. Materials and testing

The investigated 1050 H14 Al multi-layer corrugated structure was composed of 16 brazed trapezoidal zig-zag fin layers. The height, width, length and thickness of a fin are sequentially 3, 1.5, 2.5 and 0.135 mm (Fig. 1(a)). The corrugated fin layers are commercially manufactured by a local factory using a sheet-forming process. In this process, the pairs of punches and dies sequentially deform 1050 H14 Al sheet into a regular trapezoidal shape. The zig-zag form seen in Fig. 1 (b) is to enhance the heat conduction between the fin layers in a multi-layer construction. The fin layers were assembled using a

brazing process. Prior to brazing, the fin layers were subjected to a pre-treatment process composing of cleaning and fluxing. The brazed multi-layer corrugated sandwich panel shown in Fig. 2(a) is 500 × 500 × 50 mm in size and assembled in 0°/90° fin layer configuration. The face sheets prevent the mechanical damaging of the layers in brazing and subsequent machining operations. The brazing was performed by the producer in a furnace at 600° C (10 min) using a 4343 Al filler (∼7 wt%). The cylindrical test samples with and without face sheets (corrugated projectile) are shown in Fig. 2(b). These samples were extracted from the sandwich plate and the face sheets were removed using a wire electro-discharge machine. The quasi-static compression and direct impact test samples were 40 mm in diameter and 48 mm in height and had a density of 260 kg m^{-3}.

The quasi-static compression tests were carried at a nominal strain rate of 10^{-1} s^{-1}. The tests at lower strain rates were noted to increase the simulation solution time substantially. A video extensometer synchronized with the Shimadzu universal test machine was used to record the displacement. Direct impact tests were conducted in a strain-gaged modified SHPB set-up at the impact velocities of 105, 140 and 200 m s^{-1}. In these tests, the cylindrical test sample was fired at the end of the SHPB incident bar [1,2,9]. The used SHPB set-up was made of 7075 T6 Al alloy bars having a diameter the same as the test sample, 40 mm, and an incident bar length of 1000 mm. The elastic modulus and density of the bar material are 70 GPa and 2810 kg m^{-3}, respectively. The stress on the incident bar was measured by means of
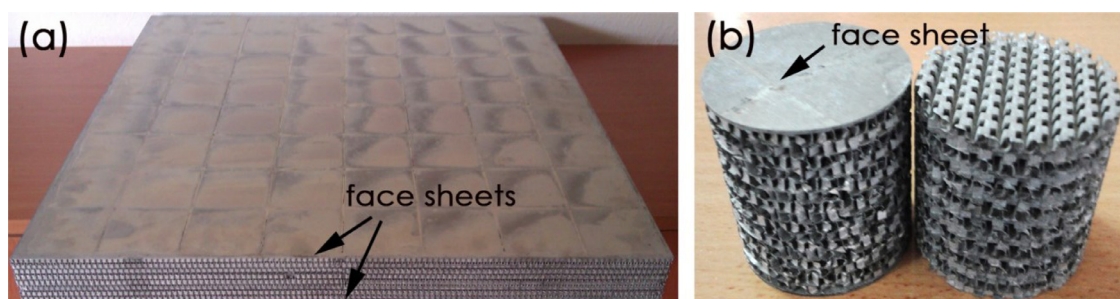

Fig. 2. (a) The brazed corrugated core sandwich panel with face sheets and (b) the cylindrical test samples (40 mm in diameter) with and without face sheets.
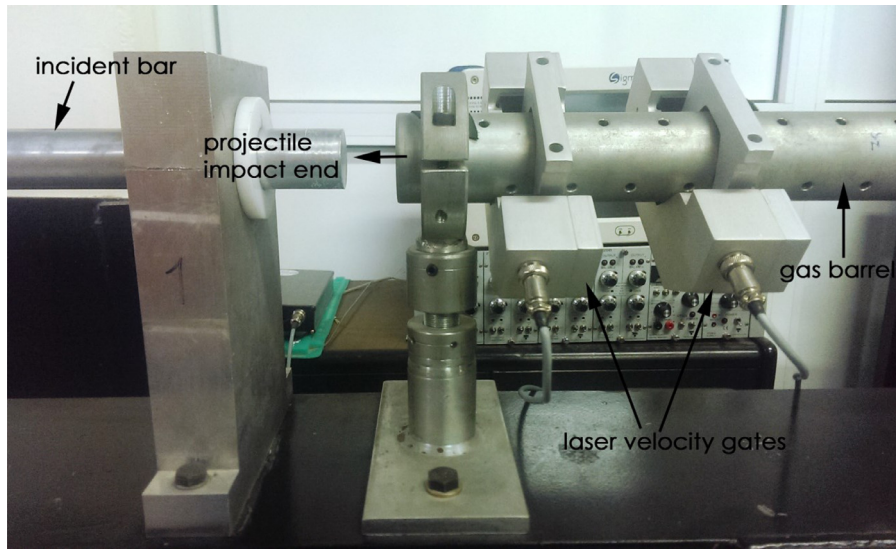
Fig. 3. The picture of the part of SHPB direct impact test set-up.

350 Ω foil strain gages in a full Wheatstone-bridge configuration. The bridge voltage was recorded with an oscilloscope. In a typical test, the cylindrical sample was inserted inside the gas barrel and the releasing the gas chamber pressure (nitrogen) propelled the sample in the barrel onto the end of the incident bar. The distance between the end of the incident bar and the location of full-bridge strain gages was 500 mm. The sample impact to the incident bar was captured by a Fastcam Photron high speed camera at 20,000 fps. The velocity of the sample was altered by varying the gas chamber pressure and measured using laser-velocity gates inserted at the exit of the gas barrel as shown in Fig. 3. The stress on the incident bar (σ) was determined using the following equation,

$$\sigma = \frac{E_b d_b{}^2 2\varepsilon_t(V)}{d_s{}^2 GKV(1+\mu)} \tag{1}$$

where E_b is the elastic modulus of the bar material and d_b and d_s are sequentially the bar and sample diameter, $\varepsilon_t(V)$ is the strain on the incident bar, G is the gain, K is the gage factor, V is the excitation voltage and μ is the Poisson's ratio of the bar material.

3. Numerical modelling

The quasi-static compression and direct impact test numerical models are shown in Fig. 4(a) and (b), respectively. The quasi-static compression test model consists of top and bottom compression test platens and the test sample (Fig. 4(a)). The test platen model contained 38,400 rigid solid elements. The translational and rotational motions of the bottom compression platen are restricted in all directions except the translational motion of the top platen in the z-direction (4.8 mm s^{-1}). The test sample was modelled using Four-node Belytschko–Tsay shell elements with five integration points. The effect of mesh size was investigated using three different element sizes in the quasi-static compression simulations. These are coded as (i) fine mesh consisting of 1,164,168 shell elements (0.25 × 0.25 mm), (ii) medium mesh consisting of 527,176 shell elements (0.375 × 0.375 mm) and (iii) coarse mesh consisting of 87,350 shell elements (0.75 × 0.75 mm). A bending type of imperfection determined through extensive microscopic observations of individual fin walls having a length of 3 mm, a radius of 1.4 mm and inclined with an angle of 26.92° to the original fin wall was introduced to the fin walls of individual layers. The imperfection was only introduced into layer 5 and layer 11 from top to bottom, which corresponded to the initial collapse layers of the quasi-static compression

test sample. It was numerically found that the direct impact test stresses were imperfection insensitive; therefore, the direct impact tests were implemented using the perfect model. The imperfection insensitive dynamic crushing was also reported previously in a corrugated structure [22]. A part of full geometrical model of the SHPB direct impact test is shown in Fig. 4(b). The corrugated structure material, 1050 H14 aluminum alloy, was modelled with MAT_SIMPLIFIED_JOHNSON_COOK (Material type 98) material model. The equivalent stress (σ_y) in the Johnson and Cook (JC) flow stress model is given as [23],

$$\sigma_y = \left[A + B\varepsilon_p^n\right]\left[1 + C\,ln\dot{\varepsilon}_p^*\right]\left[1 - T_H^m\right] \tag{2}$$

where, ε_p is the equivalent plastic strain, $\dot{\varepsilon}_p^*$ is the equivalent plastic strain rate ratio and T_H is the normalized temperature. Since the material type 98 does not take into account the temperature effect and aluminum alloys are known to have negligible strain rate dependent flow stress, only first bracket of Eq. (2) is taken into account. The material model parameters of the heat-treated 1050 H14 Al (the sample was heat treated at 600 °C for 10 min with the same heating and cooling rates used in the brazing process) were determined previously and reported as $A = 24$ MPa, $B = 154.3$ MPa, $n = 0.32$ with a fracture strain of 0.86 [24]. The incident 7075 T6 Al bar was modelled using 50,400 4-node constant stress solid elements and MAT01_ELASTIC material model. The longitudinal elastic wave speed of the bar material was 5091 m s^{-1}; therefore it took 600 μs for a compression wave to return back as tensile wave from the other end of the incident bar. Only the axial movement of the incident bar in the z-direction was allowed in the model. The contact between the bar and sample was defined by AUTOMATIC_SURFACE_TO_SURFACE contact. The incident bar stress was numerically determined from an element 500 mm away from the impact end, the same as the tests. The contact between the fin layers of the corrugated sample was defined by AUTOMATIC_SINGLE_SURFACE contact algorithm. Since the total CPU time of the quasi-static simulation was relatively long [25], mass scaling was applied by defining a positive time step in CONTROL_TIMESTEP card. The static and dynamic friction coefficients at the contacts were set to 0.3 and 0.2, respectively.

4. The r-p-p-l model

Fig. 4(c) shows the numerical models of the cylindrical test sample before and after the impact to the incident bar (with a mass of M). The sample has initially an infinite elastic modulus, a constant
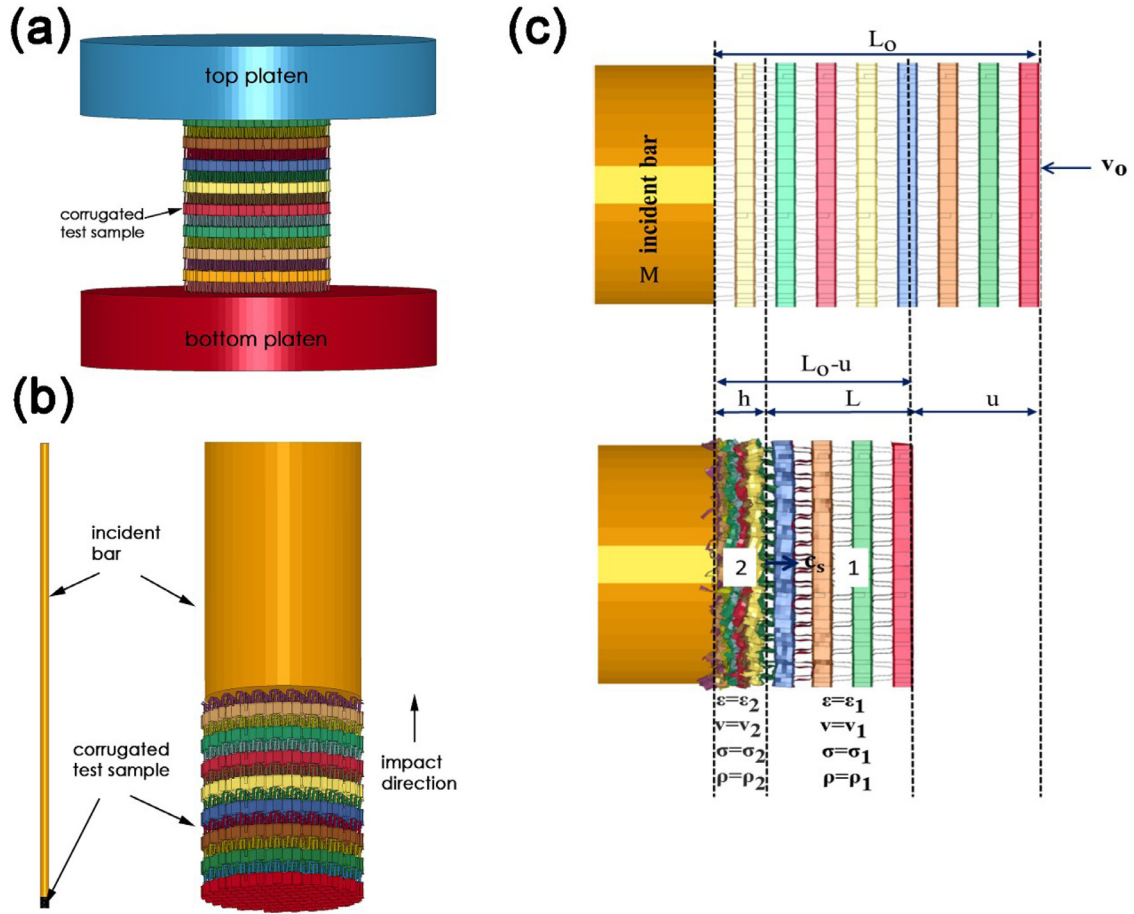
Fig. 4. The numerical model of (a) quasi-static compression and (b) direct impact SHPB test and (c) the schematic of the shock deformation.

plateau stress of σ_p, a densification strain of ε_d, an initial density of ρ_o, an initial length of L_o, a mass of m and an initial velocity of v_o. After the impact, a shock front travels through the sample with a velocity of $c_s(t)$, creating two distinct deformation regions: the region behind the shock front (2) and the region ahead of shock front (1) (Fig. 4(c)). The front and distal regions have the particle velocities of $v_2(t)$ and $v_1(t)$ and the stresses of σ_2 and σ_1, respectively. The mass and momentum conservations behind and ahead of the shock front give the following relations by taking the velocity behind the shock front zero,

$$\rho_1(c_s - v_1) = \rho_2(c_s) \tag{3}$$

And

$$(\sigma_2 - \sigma_1) = \rho_1(v_1 - c_s)v_1 \tag{4}$$

The stress behind the shock front is

$$\sigma_2 = \sigma_1 + \rho_o c_s v_1 \tag{5}$$

where, $\rho_2 = \frac{\rho_o}{1 - \varepsilon_d}$, $\rho_1 = \rho_o$, $v_1 = v$ and $c_s = \frac{\rho_1 v_1}{\rho_1 - \rho_2}$. Inserting the values of ρ_1, c_s and ρ_2 into Eq. (5) yields the stress behind shock front (peak stress) as

$$\sigma_2 = \sigma_1 + \frac{\rho_o v_o^2}{\varepsilon_d} \tag{6}$$

The momentum change between the crushed and uncrushed portion of the sample gives the particle velocity as,

$$v = \frac{du}{dt} = \sqrt{v_o^2 + \frac{2\sigma_1 \varepsilon_d}{\rho_o} \ln\left(1 - \frac{u}{\varepsilon_d L_o}\right)} \tag{7}$$

where u is the sample displacement. Inserting Eq. (7) into Eq. (6) gives the following relation for the stress behind the shock front as function of time,

$$\sigma_2(t) = \sigma_1 + \frac{\rho_o}{\varepsilon_d}\left[v_o^2 + \frac{2\sigma_1 \varepsilon_d}{\rho_o} \ln\left(1 - \frac{u}{\varepsilon_d L_o}\right)\right] \tag{8}$$

Eq. (7) is numerically integrated to determine t as function of u as,

$$t = \int_0^u \frac{du}{\sqrt{v_o^2 + \frac{2\sigma_1 \varepsilon_d}{\rho_o} \ln\left(1 - \frac{u}{\varepsilon_d L_o}\right)}} \tag{9}$$

The final displacement or arrest distance (u_f) of the sample is

$$u_f = \varepsilon_d L_o \left[1 - e^{\left(\frac{-v_o^2 \rho_o}{2\sigma_1 \varepsilon_d}\right)}\right] \tag{10}$$

The arrest distance varies between 0 and $\varepsilon_d L_o$. Note that inserting the full compaction of the sample, $u_f = \varepsilon_d L_o$, into Eq. (9) results in an infinite time. This shows that the shock generated is arrested before it reaches the end of the sample. The arrest time (τ) is given as

$$\tau = \frac{u_f}{v_o} \tag{11}$$

5. Results and discussion

4.1. Quasi-static experimental and numerical results

The experimental quasi-static (10^{-1} s^{-1}) compression stress-strain curves of four samples are shown together in Fig. 5(a). As seen
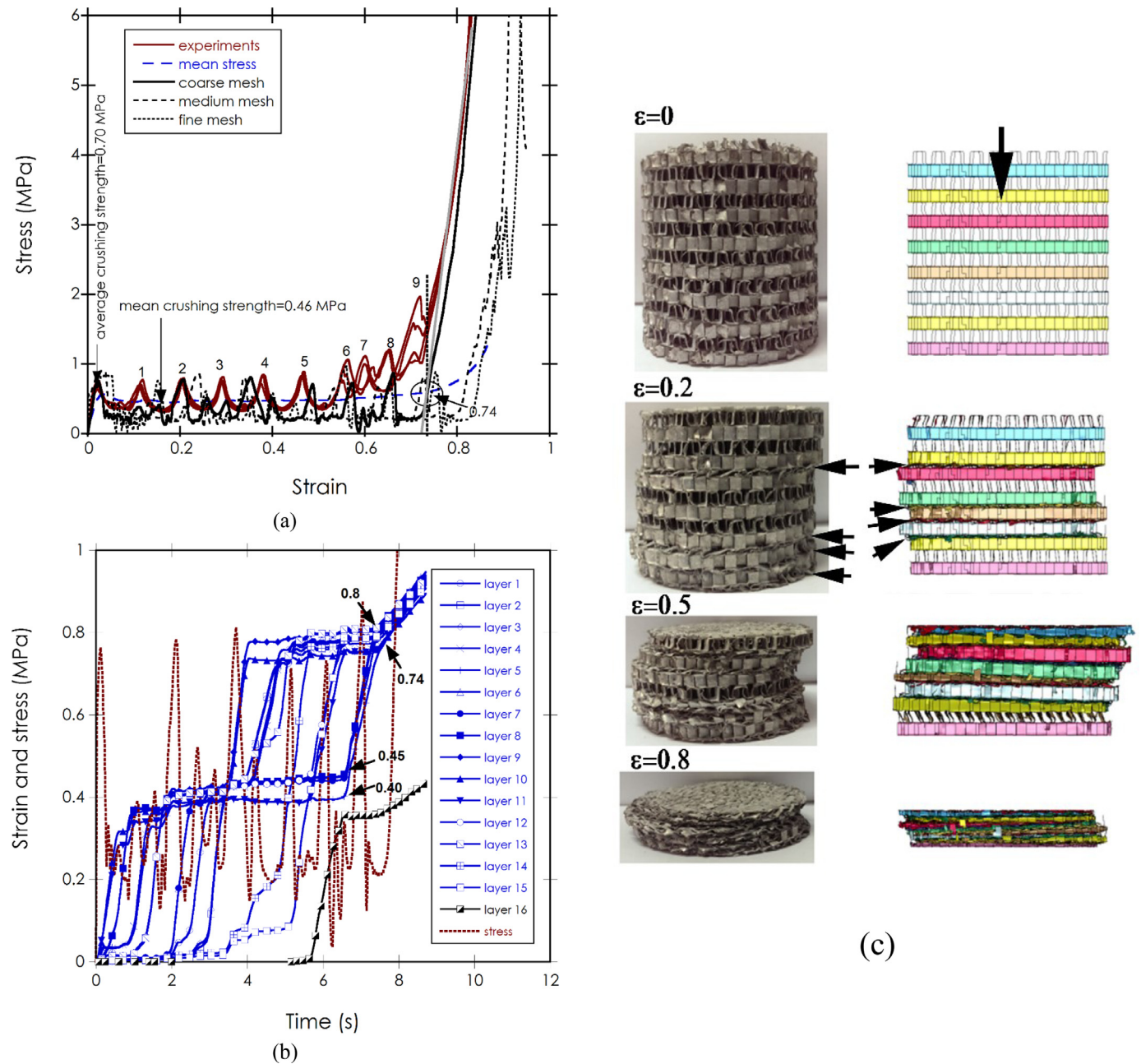
Fig. 5. (a) The quasi-static experimental and simulation stress-strain curve, (b) the simulation quasi-static layer strain-time curves and (c) the quasi-static experimental and simulation deformation pictures of the corrugated sample.

in the same figure, the stress-strain curves are repeatable and exhibit the characteristics of the compression stress-strain curves of the metallic cellular structures. The stress increases abruptly after a densification strain following a long plateau region of stress oscillations [26]. The average crushing strength (initial peak stress) and mean crushing strength are determined 0.7 MPa (0.64–0.76 MPa) and 0.46 MPa, respectively (Fig. 5(a)). The experimental quasi-static densification strain was calculated by the intercept method. In this method, a tangent line is drawn to the densification part of the stress-strain curves and the intercept of this line with the mean crushing stress is taken as densification strain. This method gives an experimental densification strain of 0.74 as marked with a circle in Fig. 5(a). The coarse, medium and fine mesh simulation quasi-static stress-strain curves are also shown in Fig. 5(a) for comparison. Both the experimental initial crush strength and the densification strain are well predicted using a coarse mesh model as seen in Fig. 5(a). It

is also noted that the coarse mesh simulation stress-strain curve exhibits similar trends with the experimental curve, except the simulation stress-strain curve shows no stress increase near densification region and relatively lower stress valleys in the plateau region (Fig. 5(a)). The simulation fin layer strain-time and stress-time histories of the quasi-static test are shown in Fig. 5(b). In this figure, the layer next to the cross-head is coded as 1 and the layer next to the bottom plate as 16. Two-stage compression of the fin layers is noted in Fig. 5(b). The layers are initially compressed (not progressively) to 0.40–0.45 strain, thereafter to 0.74 and 0.8 strain as marked with the arrows in Fig. 5(b). The quasi-static numerical densification is therefore taken as 0.77 as the average of 0.74 and 0.8 and used in the r-p-p-l model calculations. The fin wall collapse initiates in layer 11 and layer 10 concurrently, then sequentially layer 8-layer 9 and layer 5-layer 4 collapse. The last three layers, layer 14, 15 and 16 are compacted to the densification strain in the second stage. The
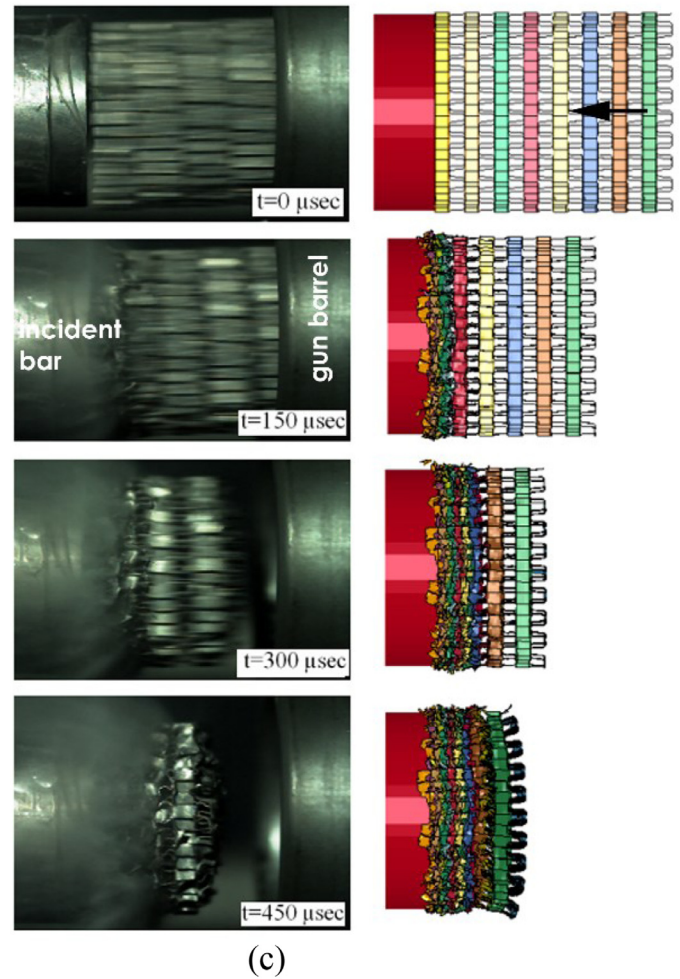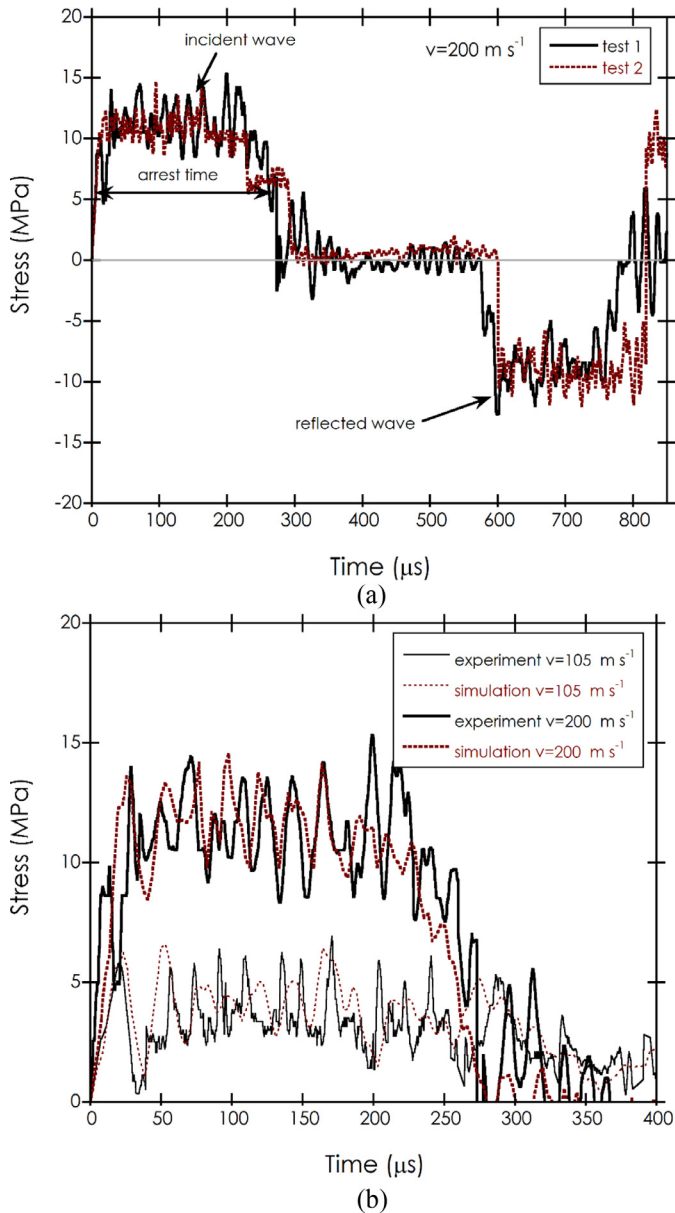
Fig. 6. (a) The experimental stress-time history of the corrugated sample at 200 m s^{-1}, (b) the experimental and numerical stress-time history at 105 and 200 m s^{-1} and (c) direct impact (150 m s^{-1}) experimental and simulation deformation pictures of the sample.

experimental and simulation quasi-static deformation pictures of the corrugated sample are shown in Fig. 5(c) at various strains. The experimental and simulation deformations as noted in Fig. 5(c) proceed with the discrete, non-contiguous bands of crushed (shearing and partly bending) fin layers. The experimental and simulation initial fin wall crushing starts from the layers at/near layer 11 and layer 5 as marked with the arrows in Fig. 5(c). As mentioned earlier, a bending imperfection is intentionally inserted into layer 5 and layer 11 in order to start the numerical fin wall crushing from the same layers as the experiment. It is noted experimentally and numerically that two or more fin layers collapse concurrently at the quasi-static strain rate. As a result of this, only 9-10 peaks (after initial peak) are seen in the stress-strain curve (numbered in Fig. 5(a) and also see Fig. 5(b)) despite to the fact there are 16 fin layers. It is noted in Fig. 5(a) that the experimental crushing stress increases gradually after about 0.4 strain until about the densification strain. The stress increase occurs at the later stages of the deformation after the crushing of 9-12 fin layers; then the uncrushed and partially crushed

layers are compressed altogether. The increased experimental crushing stress near the densification and the experimental higher stress valleys are attributed to the filler material used in the brazing. The filler increases the thickness of the fin walls at the top and bottom of the layers. The effect of filler material on the crushing behaviour will be investigated in another study.

## 4.2. Direct impact experimental and numerical results

The experimental stress-time histories of two samples tested at 200 m s^{-1} are shown in Fig. 6(a). The tests show very similar stress-time profiles to each other. The stress wave starting at about 600 μs and marked with an arrow in Fig. 6(a) is due to the reflected tensile wave from the end of the incident bar. The arrest time is calculated between the halfway of initial increasing and final decreasing part of the stress-time curves as shown in Fig. 6(a)). The experimental and simulation stress-time curves at 105 and 200 m s^{-1} are shown in Fig. 6(b) for comparison. The experimental and simulation stress-
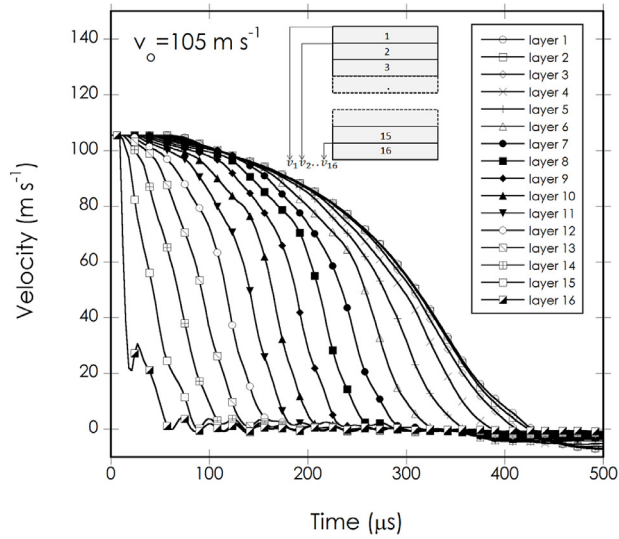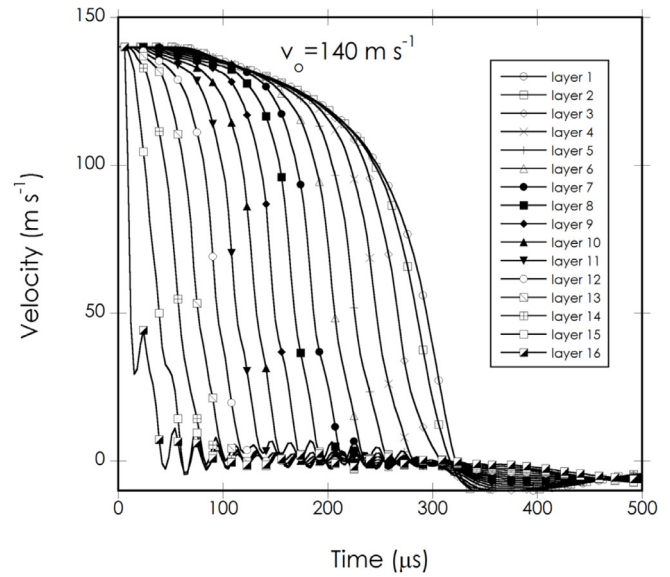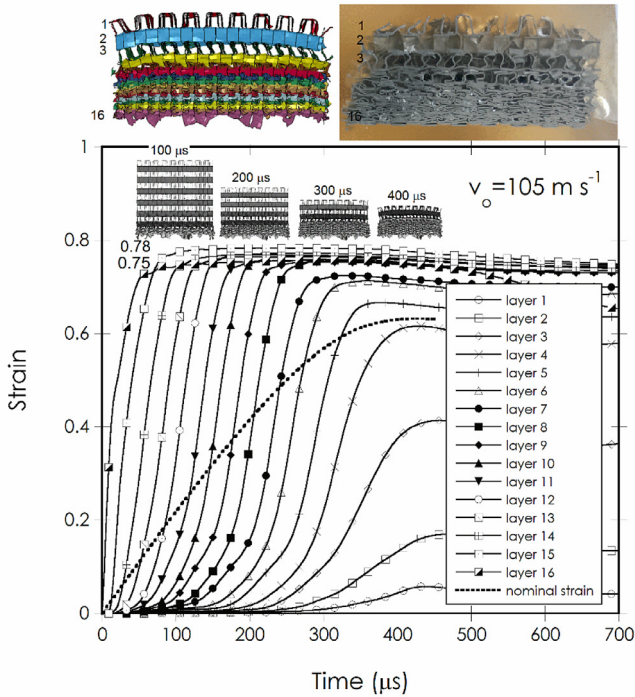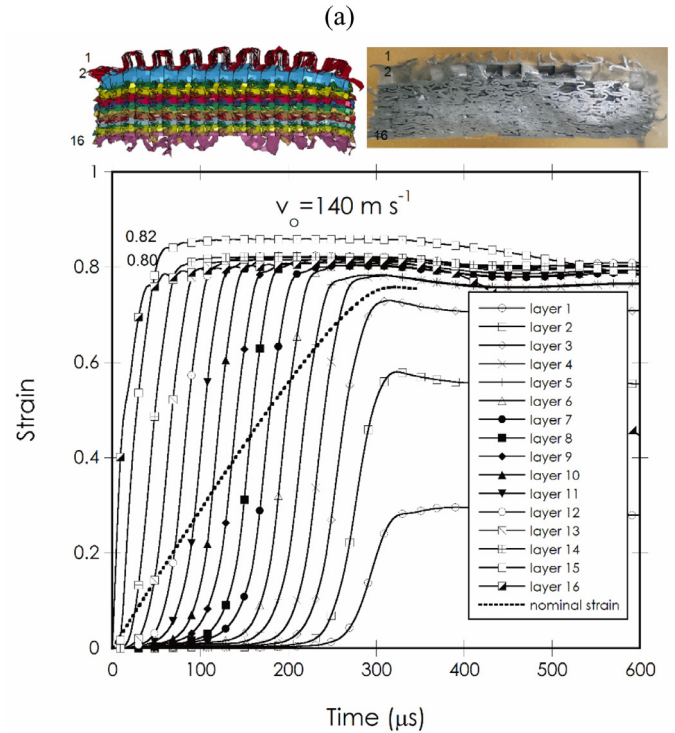
Fig. 7. The simulation (a) velocity and (b) layer strain-time curves at 105 m s^{-1}.

Fig. 8. The simulation (a) velocity and (b) layer strain-time curves at 140 m s^{-1}.

time profiles as seen in the figure are very similar to each other. Following the initial elastic region, the stress reaches a peak or plateau stress. The wave is arrested after a plateau region of stress oscillations. The peak/plateau stress is reached, depending on the impact velocity, both experimentally and numerically in about 20–40 μs. The direct impact experimental and simulation deformation pictures of the sample tested at 105 m s^{-1} are shown in Fig. 6(c). The exposure time of each high speed camera record in Fig. 6(c) is 150 μs corresponding to a total duration of 450 μs. As opposite to the quasi-static deformation (Fig. 5(c)), the direct impact deformation proceeds with the sequential, in-planar crushing of the fin layers starting from proximal end (the impact end) as seen in Fig. 6(c), showing a shock deformation characteristic. Several different formulations were previously developed to calculate the critical velocity for shock formation in cellular structures [11,27,28]. The critical velocity in

present study is calculated using the following relation which considers all the internal energy is due to the loss of the kinetic energy [15],

$$v_{cr} = \sqrt{\frac{2\sigma_1 \varepsilon_d}{\rho_o}} \qquad (12)$$

Taking $\sigma_1 = 0.7$ MPa, $\rho_o = 260$ kg m^{-3} and $\varepsilon_d = 0.77$, Eq. (12) yields a critical velocity of 64 m s^{-1} for the investigated corrugated structure. Above this velocity, the shock formation is expected. The velocities investigated, 105, 140 and 200 m s^{-1}, are therefore well above the calculated critical velocity.

Above the critical velocity, the densification strains are determined numerically by tracking the individual fin layer strains at each velocity. Figs. 7(a) and (b) show the simulation velocities and
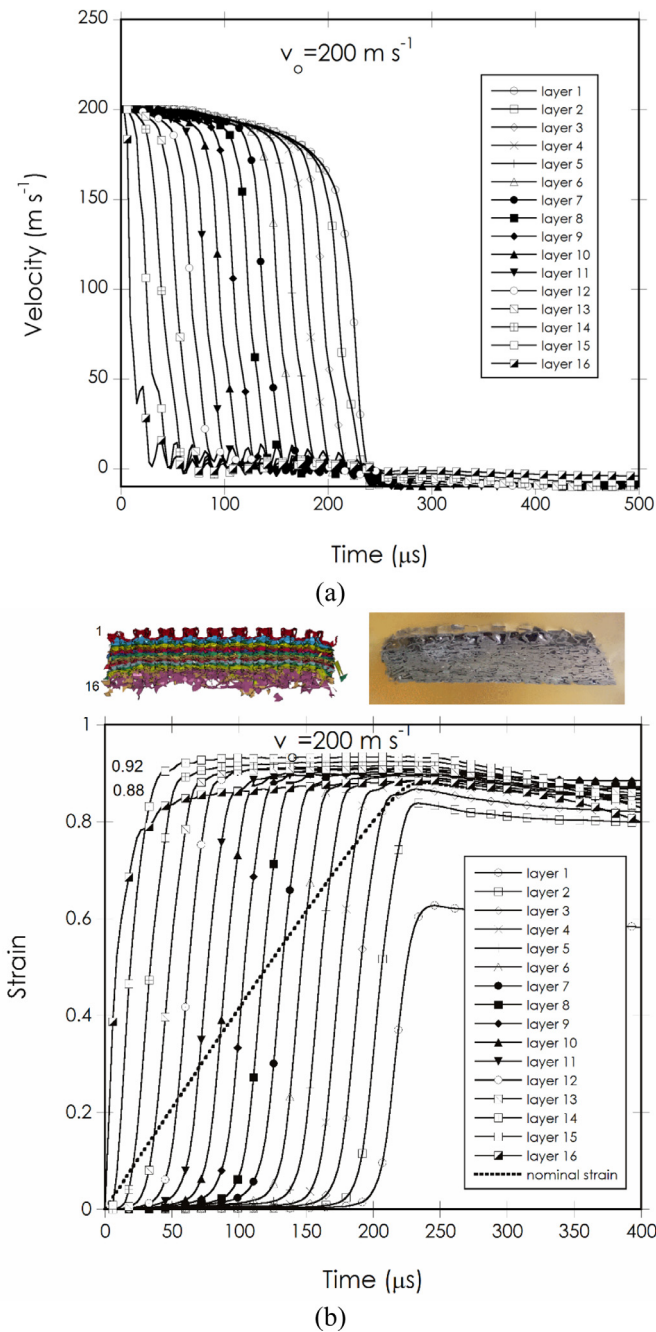
(a)

(b)

Fig. 9. The simulation (a) velocity and (b) layer strain-time curves at 200 m s^{-1}.

(a)

(b)

Fig. 10. The layer strain vs. time curves at (a) 50 and (b) 75 m s^{-1}.

strains of the layers as function of time for the sample tested at 105 m s^{-1}, respectively. The proximal end layer (impact end) of the sample is numbered as 16 and the distal end layer as 1 as shown in the inset of Fig. 7(a). It is noted in the same figure that the distal end layer has the longest duration of velocity, while the proximal end layer the lowest, as the layers near the proximal end collapse at the earliest stage of the impact. The velocity-time profiles of the first three layers (distal end) are noted to be very much similar, while the velocity-time profiles of the following layers show distinct differences between each other as seen in Fig. 7(a). The final strain attained in layer 1 shown in Fig. 7(b) is the lowest (0.06), while it gradually increases to 0.75 until layer 8. The densification strains in the fully compacted layers vary between 0.75 and 0.78, similar to those of quasi-static test. When the impact velocity increases to 140 m s^{-1}, the durations of the velocities are shortened (Fig. 8(a)); the first layer
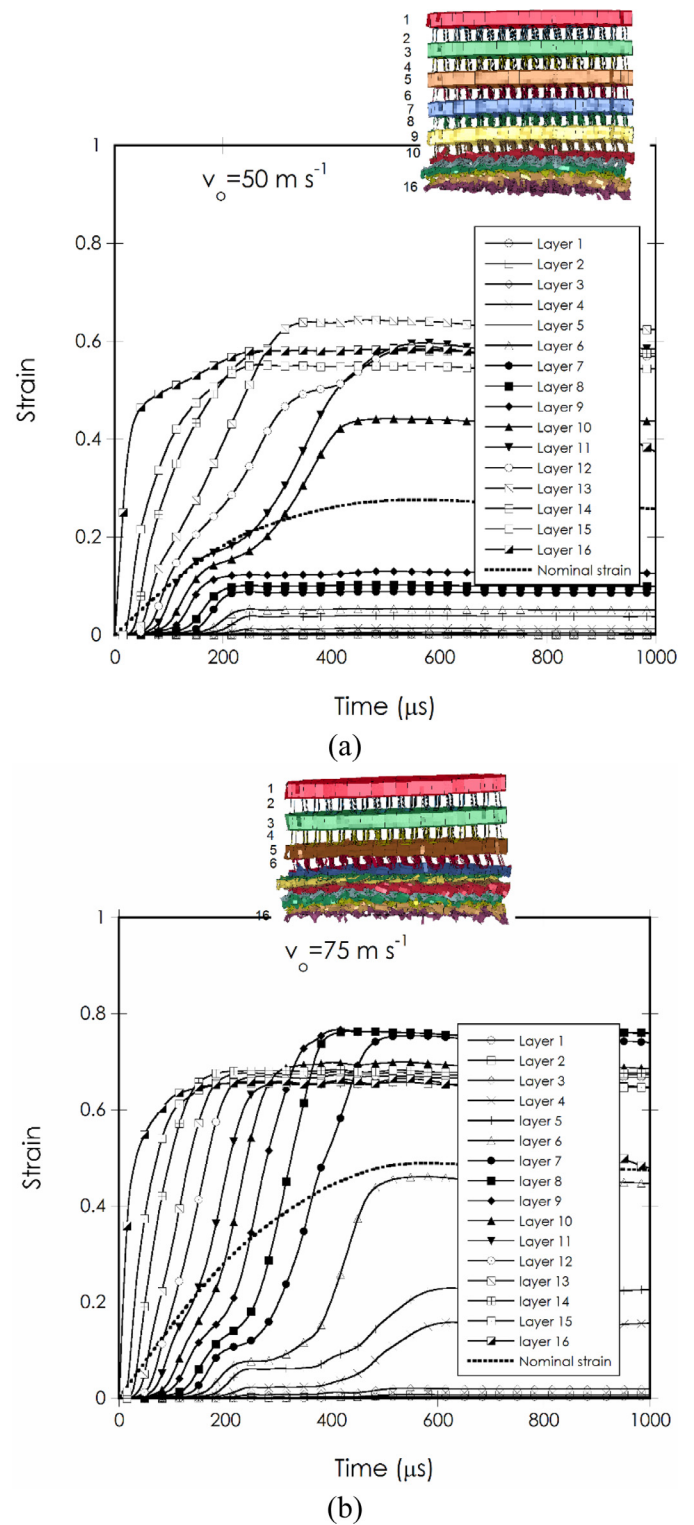
strain increases to 0.29 and the strain values saturate at about 0.80 after layer 6 (Fig. 8(b)). The densification strains of the fully compacted layers vary between 0.80 and 0.82 as shown in Fig. 8(b). When the velocity increases to 200 m s^{-1}, the durations of the velocities are further shortened (Fig. 9(a)); the first layer strain increases to 0.63 and the layer strains saturate at about 0.88–0.92 strain after layer 3 (Fig. 9(b)). At all impact velocities, the densification strain of the proximal end layer, layer 16, is slightly lower than that of the

following layers as it is the free end. The variations of the nominal strain with time are also shown in Fig. 7(b) for 105 m s⁻¹, in Fig. 8(b) for 140 m s⁻¹ and in Fig. 9(b) for 200 m s⁻¹. The final nominal strain is lower than the layer densification strains at 105 and 140 m s⁻¹, while it nearly reaches the layer densification strains at 200 m s⁻¹. This also confirms the full compaction of the fin layers at 200 m s⁻¹. The experimentally and numerically deformed cross-sectional views of the samples are also found very much similar at all velocities and shown at the top of Figs. 7(b), 8(b) and 9(b). Although, the initiation and progression of the fin layer collapse are sequential, the first 3 layers are noted to be compacted to the final strains far below the densification strain at 105 m s⁻¹ (numbered in Fig. 7(b)), the first 2 layers at 140 m s⁻¹ (numbered in Fig. 8(b)) and the first layer at 200 m s⁻¹ (numbered in Fig. 9(b)). The layer compaction profile becomes completely different when the impact velocity is near or below the subcritical velocities. The strain-time profile at 50 m s⁻¹ is mostly diffusive although an intense deformation of the layers occurs near the proximal end (Fig. 10(a)).The layer crushing is also noted to be not sequential: layers deform to a larger and lower extend together at a given deformation time. This diffusive nature of the strain becomes more pronounced following the last three-four layers of the intense deformation region at the proximal end. The diffusive nature of the strain is somewhat reduced when the velocity increases to 75 m s⁻¹ (Fig. 10(b)). At this velocity, the shock deformation nature is seen in the last 5 layers at the proximal end and the strain gradually becomes diffusive in the following layers. The impact deformation at this velocity reflects a transition stage from non-sequential, diffusive to sequential, progressive crushing. The low compaction strains attained in the layers at these velocities also resemble near quasi-static type of deformation, but note that the full compaction or densification strains of the layers has not been reached.

4.3. The analysis of the results of the r-p-p-l model

Fig. 11 shows the experimental, simulation and r-p-p-l model stress-time curves at three different velocities. The r-p-p-l model stress-time curves are calculated using the quasi-static densification strain of 0.77 and crushing strength of 0.7 MPa. The simulation stress is 20 MPa shifted in the same figure. The r-p-p-l model gives similar stress-time profiles with the experiments and simulations at 105
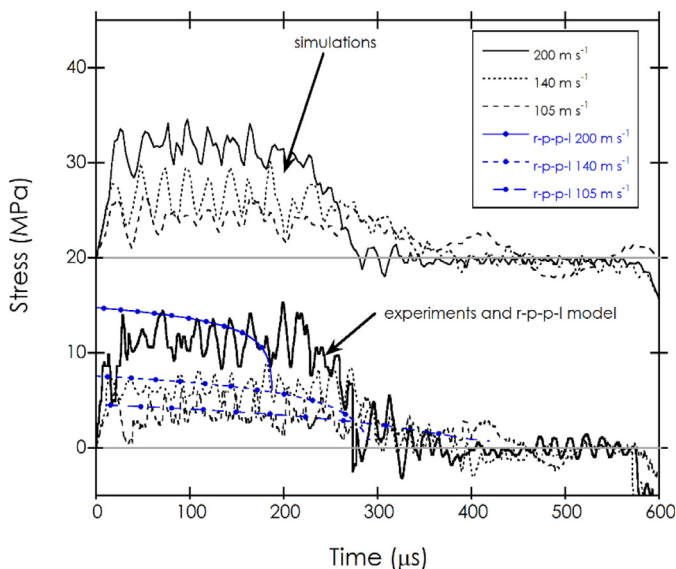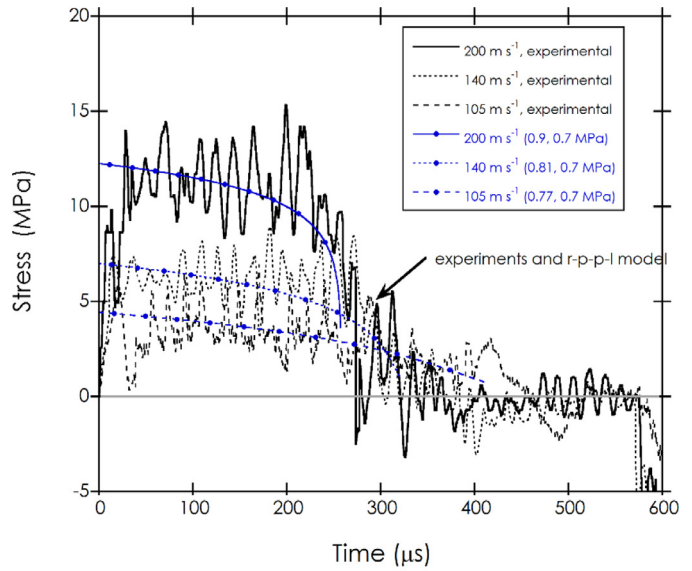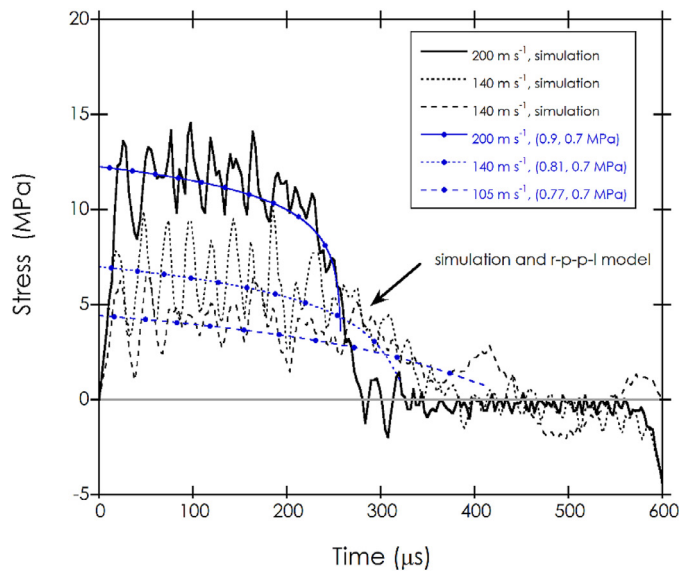

Fig. 11. The experimental, simulation and the r-p-p-l model predicted bar stress-time curves.

(a)

(b)

Fig. 12. The comparison of the numerically determined densification strain r-p-p-l model stress-strain curves with those of (a) experimental and (b) simulation stress-time curves.

and 140 m s⁻¹, while it results in relatively shorter duration and higher stresses at 200 m s⁻¹ (Fig. 11). When the numerically determined varying average densification strains are implemented, the r-p-p-l model however well predicts the experimental and simulation stress-time profiles as shown in Figs. 12(a) and (b), respectively. It predicts a peak stress of 4.42 MPa and a loading duration of 413 μs at 105 m s⁻¹. The peak and mean stresses are sequentially 6–6.5 MPa, 3.94–4.33 MPa and 390-400 μs experimentally and 6.6 MPa, 4.35 MPa and 405 μs numerically. The small discrepancies between the model and experimental and simulation stresses and durations may arise from several reasons. The sample is assumed to be perfectly plastic in the r-p-p-l model. This may lead to shorter loading durations. A planar impact is also assumed in the model, while an ideal planar impact in the experiments is hardly possible.

Fig. 13 shows the simulation stress-nominal strain curves at the velocities between 25 and 200 m s⁻¹. The simulation and experimental mean stresses were determined after the initial
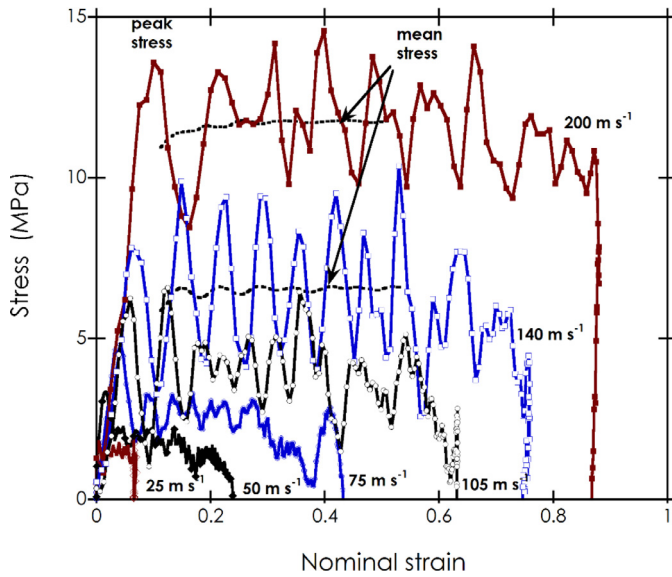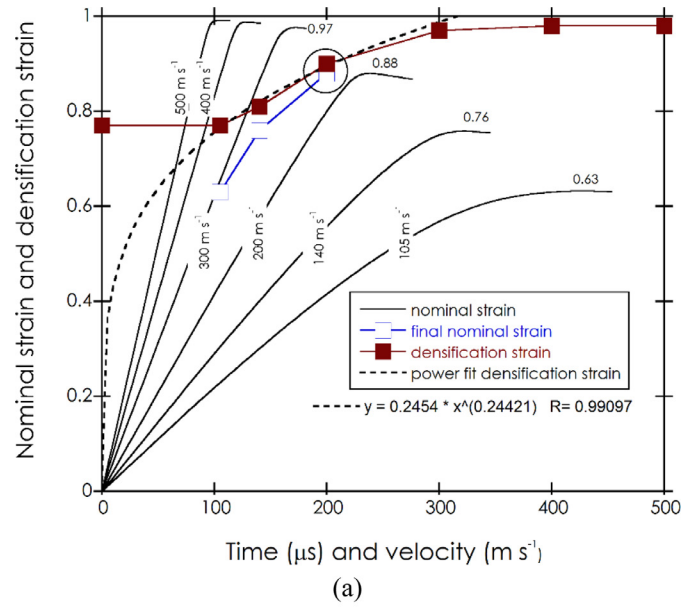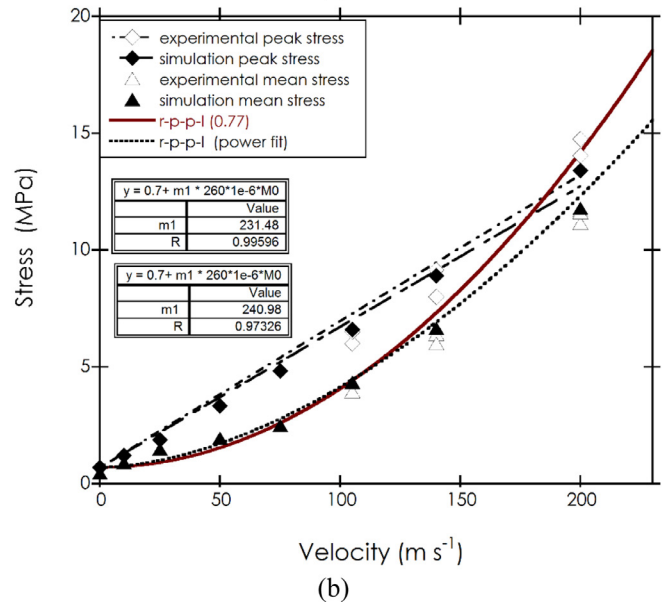
Fig. 13. The simulation stress vs. nominal strain at increasing velocities.

peak stress and the simulation mean stresses are shown in Fig. 13 for 140 and 200 m s^{-1} tests. The simulation stresses, mean stresses and final attained strains increase as the velocity increases as shown in Fig. 13. Fig. 14(a) shows the variation of simulation nominal strain with time and the densification strain with the velocity. The densification strain in the same graph is fitted with a power law relation between 105 and 200 m s^{-1}. As the velocity increases to and above 300 m s^{-1}, the final nominal strain reaches the densification strain and the densification strain saturates at about 0.97, corresponding to the full compaction of the corrugated sample. The experimental and simulation initial peak and mean stresses at different impact velocities until about 200 m s^{-1} are shown in Fig. 14(b). The r-p-p-l model stresses determined by using 0.77 quasi-static densification strain is also shown in the same figure. The r-p-p-l model based on the quasi-static densification strain overestimates the experimental and simulation mean stresses after about 100 m s^{-1} and underestimates the initial peak stresses below 200 m s^{-1}, while it nearly predicts the peak stresses at 200 m s^{-1}. The experimental and simulation peak stresses are well fitted with a linear relation to the impact velocity, while the mean stresses are well fitted with the r-p-p-l model stress based on power law-fit to the numerically determined densification strains. The r-p-p-l model under estimation of the peak stresses at low velocities was previously reported for wood [1], aluminum foams [6] and aluminum honeycombs [8]. It was proposed that the micro inertial effects were responsible for the increase of the collapse stress at and below subcritical velocities while above the critical velocities the shock deformation [1,8,11,12]. The structures exhibiting a relatively flat-topped quasi-static load displacement curve are classified as Type I, while the structures exhibiting a steeply declining quasi-static load-displacement curve following an initial peak load are classified as Type II structure [29]. Type II structure are more inertia and strain rate sensitive than Type I structures. The deformation of Type II structures was shown to occur in two phases: plastic compression and the rotations of plastic hinges [30]. It was reported that the inertia is dominant in the first phase. The corrugated structures tested in the present study also show inertia-sensitive Type II behaviour as reported previously [18]. The propagation of the plastic wave at high strain rates suppresses the more compliant bending modes and hence increases the crushing stress [31]. The peak stress was also shown previously

(a)

(b)

Fig. 14. The variation of the nominal strain with time and the numerically determined densification strain with velocity and (b) the experimental, simulation and r-p-p-l model peak and mean stresses vs. velocity.

to vary linearly with the velocity particularly at low velocities which was attributed to the axial plastic wave propagation in the cellular material walls which preceded the progressive collapse mechanism [2,7,12]. The peak stress is therefore fitted to the following relation,

$$\sigma_2 = \sigma_1 + \rho_o c_p v_1 \tag{13}$$

where c_p is the plastic wave velocity of the cell wall material. A liner fit to the experimental peak stresses in Fig. 14(b) gives a plastic wave velocity of 231 m s^{-1}. For the studied Al alloy, the determined plastic wave velocities (from stress-strain curve) are 235, 200 and 185 m s^{-1} at 0.2, 0.3 and 0.4 strain, respectively. A plastic wave velocity of 161 m s^{-1} was previously reported for a 6061-T6 Al alloy [12].

Fig. 15(a) shows the simulation stress-time curves up to 500 m s^{-1}. In the same figure, the r-p-p-l model stress-time curves based on the constant quasi-static densification strain (0.77) and numerically determined varying densification strains (0.77-0.97) are
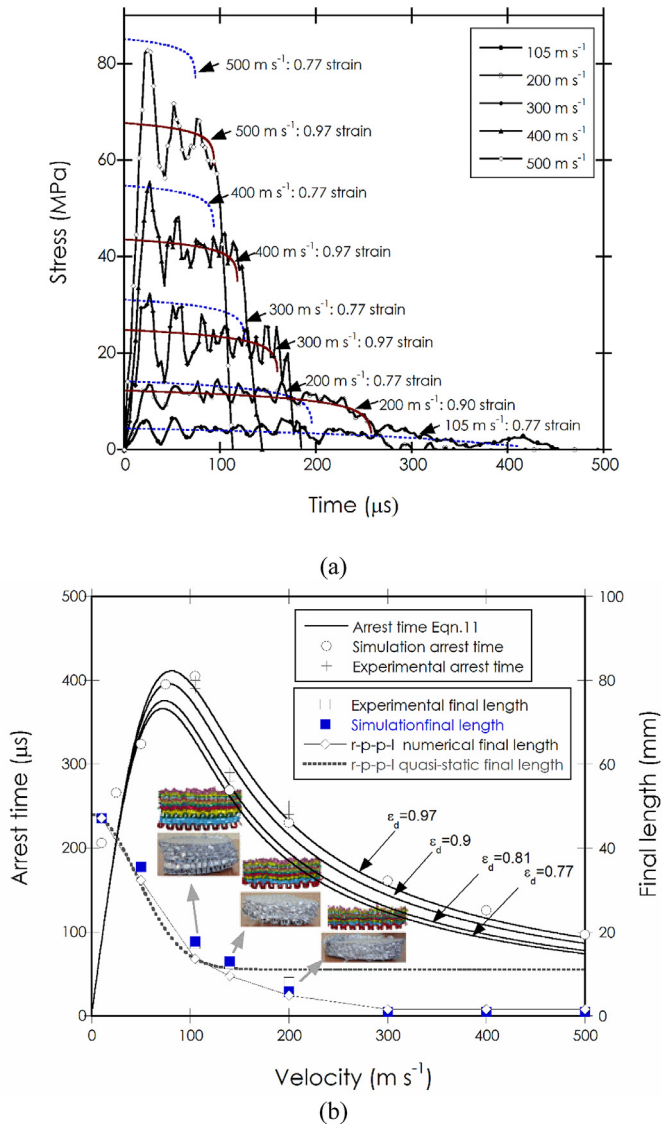
Fig. 15. (a) The simulation and r-p-p-l model predicted stress-time histories at the velocities between 105 and 500 m s^{-1} and (b) the experimental, simulation and r-p-p-l model arrest time and experimental and simulation final thicknesses as function of velocity.

also shown. It is seen in Fig. 15(a) that the r-p-p-l model based on the quasi-static densification strain nearly predicts the peak stresses at and above 200 m s^{-1}, while the r-p-p-l model based on the numerically determined densification strains show well agreements with the mean stresses or plateau stresses at all velocities. In order to show fidelity of the used numerical model, the experimental, numerical and r-p-p-l model arrest times and final thicknesses are shown for comparison in Fig. 15(b) as function of the velocity. The r-p-p-l model arrest times of the different densification strains, 0.81, 0.9 and 0.97, are also drawn in the same figure. The r-p-p-l model nearly predicts the simulation and experimental arrest times above the critical impact velocities, while it under predicts at and below the subcritical velocities. The r-p-p-l model based on the quasi-static densification strain however results in slightly lower final lengths than the simulations and experiments, while the r-p-p-l model based on the numerically determined densification strains show well correlations with the simulation and experimental final lengths above the critical velocities. The densification strain is expected to vary within the individual layers during a test, as the velocity decreases. Since the r-p-p-l model uses a constant densification

strain, the variation of the densification strain is not taken into account. The reduced nature of densification strain during a test may result in longer final lengths than those predicted by the r-p-p-l model. The r-p-p-l model final lengths based on the numerically determined densification strain are sequentially 13.6, 9.6 and 4.9 mm for 105, 140 and 200 m s^{-1}. These values are 17.7, 12.9 and 5.7 mm and 17.2, 12.3 and 8 mm for the simulations and experiments, respectively. The discrepancy between simulation and experimental final lengths particularly at the highest velocity, 200 m s^{-1}, is attributed to the fracturing/cracking of the brazing filler material during or after the test, leading to the separation/opening of the compacted layers and hence increasing the final length.

6. Conclusions

A 1050 H14 Al corrugated structure composed of brazed 16 trapezoidal zig-zig fin layers was direct impact tested in a modified SHPB at 105, 140 and 200 m s^{-1} above the critical velocities for shock deformation (~64 m s^{-1}). The stress-time histories of the direct impact tests were verified by the simulations in the explicit finite element code of LS-DYNA. The fully modelling of the corrugated structure allowed the monitoring the velocity and strain histories of each individual fin layers. A determined fin wall bending imperfection was placed into the prescribed fin layers in the quasi-static model in order to accurately simulate the quasi-static test, while an imperfection insensitive crushing stress was found in the direct impact tests. Once the fidelity of the used model was verified, the direct impact tests were extended to lower and higher velocities up to 500 m s^{-1}. The experiments and simulations showed that the deformation of the corrugated sample switched from discrete, non-contiguous bands of crushed fin layers at quasi-static velocities to sequential, in-planar crushed fin layers above the critical velocities. The layer compaction in the direct impact tests started from the impact end, showing shock type deformation. The crushing strength was shown velocity dependent and the densification strain increased with the increasing impact velocities above the critical velocities. The r-p-p-l model based on the quasi-static densification strain well predicted the peak stresses at and above 200 m s^{-1}, while the r-p-p-l model based on the numerically determined varying densification strains showed well correlations with the mean stresses at all velocities. Both models however underestimated the peak stresses below 200 m s^{-1}. It was proposed that the micro inertial effects were responsible for the increase of the collapse stresses at and below subcritical velocities, while shock deformation became dominant above the critical velocities.

References

[1] Reid SR, Peng C. Dynamic uniaxial crushing of wood. Int J Impact Eng 1997;19:531–70.
[2] Harrigan JJ, Reid SR, Tan PJ, Reddy TY. High rate crushing of wood along the grain. Int J Mech Sci 2005;47:521–44.
[3] Chen A, Kim H, Asaro RJ, Bezares J. Non-explosive simulated blast loading of balsa core sandwich composite beams. Compos Struct 2011;93:2768–84.
[4] Radford DD, Deshpande VS, Fleck NA. The use of metal foam projectiles to simulate shock loading on a structure. Int J Impact Eng 2005;31:1152–71.
[5] Zou Z, Reid SR, Tan PJ, Li S, Harrigan JJ. Dynamic crushing of honeycombs and features of shock fronts. Int J Impact Eng 2009;36:165–76.
[6] Tan PJ, Reid SR, Harrigan JJ, Zou Z, Li S. Dynamic compressive strength properties of aluminium foams. Part II—'shock' theory and comparison with experimental data and numerical models. J Mech Phys Solids 2005;53:2206–30.
[7] Tan PJ, Reid SR, Harrigan JJ, Zou Z, Li S. Dynamic compressive strength properties of aluminium foams. Part I - experimental data and observations. J Mech Phys Solids 2005;53:2174–205.

[8] Harrigan JJ, Reid SR, Peng C. Inertia effects in impact energy absorbing materials and structures. Int J Impact Eng 1999;22:955–79.
[9] Lopatnikov SL, Gama BA, Haque MJ, Krauthauser C, Gillespie JW, Guden M, Hall IW. Dynamics of metal foam deformation during Taylor cylinder-Hopkinson bar impact experiment. Compos Struct 2003;61:61–71.
[10] Karagiozova D, Langdon GS, Nurick GN. Propagation of compaction waves in metal foams exhibiting strain hardening. Int J Solids Struct 2012;49: 2763–77.
[11] Zheng ZJ, Yu JL, Wang CF, Liao SF, Liu YD. Dynamic crushing of cellular materials: a unified framework of plastic shock wave models,. Int J Impact Eng 2013;53:29–43.
[12] Tan PJ, Reid SR, Harrigan JJ. On the dynamic mechanical properties of open-cell metal foams - a re-assessment of the 'simple-shock theory'. Int J Solids Struct 2012;49:2744–53.
[13] Gaitanaros S, Kyriakides S. Dynamic crushing of aluminum foams: Part II - Analysis. Int J Solids Struct 2014;51:1646–61.
[14] Deshpande VS, Fleck NA. High strain rate compressive behaviour of aluminium alloy foams. Int J Impact Eng 2000;24:277–98.
[15] Tan PJ, Reid SR, Harrigan JJ, Zou Z, Li S. Dynamic compressive strength properties of aluminium foams. Part II - 'shock' theory and comparison with experimental data and numerical models. J Mech Phys Solids 2005;53:2206–30.
[16] Peroni M, Solomos G, Pizzinato V. Impact behaviour testing of aluminium foam. Int J Impact Eng 2013;53:74–83.
[17] Liu YD, Yu JL, Zheng ZJ, Li JR. A numerical study on the rate sensitivity of cellular metals. Int J Solids Struct 2009;46:3988–98.
[18] Kilicaslan C, Guden M, Odaci IK, Tasdemirci A. The impact responses and the finite element modeling of layered trapezoidal corrugated aluminum core and aluminum sheet interlayer sandwich structures. Mater Des 2013;46: 121–33.
[19] Kilicaslan C, Guden M, Odaci IK, Tasdemirci A. Experimental and numerical studies on the quasi-static and dynamic crushing responses of multi-layer trapezoidal aluminum corrugated sandwiches. Thin-Walled Struct 2014;78:70–8.
[20] Hou S, Zhao S, Ren L, Han X, Li Q. Crashworthiness optimization of corrugated sandwich panels. Mater Des 2013;51:1071–84.
[21] Hou S, Shu C, Zhao S, Liu T, Han X, Li Q. Experimental and numerical studies on multi-layered corrugated sandwich panels under crushing loading. Compos Struct 2015;126:371–85.
[22] McShane GJ, Pingle SM, Deshpande VS, Fleck NA. Dynamic buckling of an inclined strut. Int J Solids Struct 2012;49:2830–8.
[23] Johnson GR, Hoegfeldt JM, Lindholm US, Nagy A. Response of various metals to large torsional strains over a large range of strain rates 0.1. Ductile metals. J Eng Mater Technol-Trans ASME 1983;105:42–7.
[24] Kılıçaslan C, Güden M, Odacı İK, Taşdemirci A. The impact responses and the finite element modeling of layered trapezoidal corrugated aluminum core and aluminum sheet interlayer sandwich structures. Mater Des 2013;46:121–33.
[25] Santosa SP, Wierzbicki T, Hanssen AG, Langseth M. Experimental and numerical studies of foam-filled sections. Int J Impact Eng 2000;24:509–34.
[26] Ashby MF, Evans AG, Fleck NA, Gibson LJ, Hutchinson JW, Wadley HNG. Chapter 4 - Properties of metal foams. In: Ashby MF, Evans AG, Fleck NA, Gibson LJ, Hutchinson JW, Wadley HNG, editors. Burlington: Metal Foams, Butterworth-Heinemann; 2000. p. 40–54.
[27] Shen CJ, Yu TX, Lu G. Double shock mode in graded cellular rod under impact. Int J Solids Struct 2013;50:217–33.
[28] Honig A, Stronge WJ. In-plane dynamic crushing of honeycomb. Part I: crush band initiation and wave trapping. Int J Mech Sci 2002;44:1665–96.
[29] Calladine CR, English RW. Strain-rate and inertia effects in the collapse of two types of energy-absorbing structure. Int J Mech Sci 1984;26:689–701.
[30] Tam LL, Calladine CR. Inertia and strain-rate effects in a simple plate-structure under impact loading. Int J Impact Eng 1991;11:349–77.
[31] Vaughn DG, Canning JM, Hutchinson JW. Coupled plastic wave propagation and column buckling. J Appl Mech-Trans ASME 2005;72:139–46.